Low-Cloud, Boundary Layer, and Sea Ice Interactions over the Southern Ocean during Winter

CASEY J. WALL, TSUBASA KOHYAMA, AND DENNIS L. HARTMANN

Department of Atmospheric Sciences, University of Washington, Seattle, Washington

(Manuscript received 30 June 2016, in final form 19 January 2017)

ABSTRACT

During austral winter, a sharp contrast in low-cloud fraction and boundary layer structure across the Antarctic sea ice edge is seen in ship-based measurements and in active satellite retrievals from *Cloud–Aerosol Lidar and Infrared Pathfinder Satellite Observations* (*CALIPSO*), which provide an unprecedented view of polar clouds during winter. Sea ice inhibits heat and moisture transport from the ocean to the atmosphere, and, as a result, the boundary layer is cold, stable, and clear over sea ice and warm, moist, well mixed, and cloudy over open water. The mean low-cloud fraction observed by *CALIPSO* is roughly 0.7 over open water and 0.4–0.5 over sea ice, and the low-cloud layer is deeper over open water. Low-level winds in excess of 10 m s^{-1} are common over sea ice. Cold advection off of the sea ice pack causes enhanced low-cloud fraction over open water, and thus an enhanced longwave cloud radiative effect at the surface. Quantitative estimates of the surface longwave cloud radiative effect contributed by low clouds are presented. Finally, 10 state-of-the-art global climate models with satellite simulators are compared to observations. Near the sea ice edge, 7 out of 10 models simulate cloudier conditions over open water than over sea ice. Most models also underestimate low-cloud fraction both over sea ice and over open water.

1. Introduction

Sea ice, low clouds, and the atmospheric boundary layer modulate the climate of the Southern Ocean by influencing surface heat fluxes. During winter, sea ice insulates the ocean from the cold atmosphere above, reducing the rate of ocean heat loss at the surface by a factor of 10 to 100 (Gordon 1991). Low clouds and moisture emit longwave (LW) radiation downward and heat the surface, and low-level winds control the surface turbulent heat and moisture fluxes. When sea ice forms, brine is rejected, adding salt to the near-surface waters. These processes modify the buoyancy of surface waters and are responsible for deep and intermediate water formation. Roughly two-thirds of the deep water in the global ocean is formed in the Southern Ocean (Johnson 2008), making it a region of critical importance for the global overturning circulation of the ocean (Marshall and Speer 2012; Talley 2013). Surface fluxes of heat and moisture in the polar regions are intimately linked to the atmospheric boundary layer and to sea ice, are poorly observed, and are a topic of high priority for improving our understanding of polar climate and climate change (Bourassa et al. 2013).

Interactions between sea ice and boundary layer clouds have previously been studied, but focus on this topic has generally been on the Arctic. Across the Arctic basin during summer and early fall, low clouds are more abundant and optically thicker over open water than over sea ice when viewed from active satellite remote sensing products (Kay and Gettelman 2009; Palm et al. 2010) and from surface observers (Eastman and Warren 2010). On the other hand, Schweiger et al. (2008) used passive satellite retrievals and found that, during fall, regions of low sea ice concentration coincide with enhanced midlevel cloudiness and reduced low-cloud cover. Barton et al. (2012) found that the sensitivity of Arctic low-cloud fraction to variations in sea ice concentration depends on synoptic regime. For stable regimes, which support low clouds, a significant but weak covariance between sea ice concentration and cloud properties occurs during most seasons (Taylor et al. 2015). Near the sea ice edge, cold, off-ice advection is known to cause enhanced low-cloud cover; however, because of a lack of observations, previous work has focused on case studies of extreme events (e.g., Walter 1980; Renfrew and Moore 1999;

Corresponding author e-mail: Casey J. Wall, caseyw8@atmos.washington.edu

Publisher's Note: This article was revised on 12 June 2017 to update the formatting of Table 1 for clarity.

DOI: 10.1175/JCLI-D-16-0483.1

Petersen and Renfrew 2009). It has also been argued that, in the Arctic, advection of moisture in the boundary layer triggers the onset of sea ice melt (Kapsch et al. 2013) and that a warmer, moister boundary layer has amplified recent sea ice decline (Serreze et al. 2009; Screen and Simmonds 2010; Boisvert and Stroeve 2015).

Unlike the Arctic, interactions between Antarctic sea ice and boundary layer clouds have been given relatively little attention. Bromwich et al. (2012) first pointed out that the total cloud fraction observed from active satellite retrievals is about 0.1–0.2 lower in sea ice–covered regions of the Southern Ocean than over open water to the north. Fitzpatrick and Warren (2007) used ship-based measurements of downwelling solar radiation over the Southern Ocean to show that, during austral spring and summer, clouds tend to be optically thicker over open water than over sea ice. It is not clear if the relationship between low clouds and sea ice in the Arctic is similar to that in the Southern Ocean.

In this study we describe the boundary layer properties and low-cloud fraction across the Southern Ocean during winter, but with an emphasis on the marginal sea ice zone. We use satellite-based active retrievals of clouds, which provide an unprecedented view of polar clouds during winter, as well as ship-based measurements. We also use a radiative transfer model to compute estimates of the downward flux of LW radiation near the sea ice edge and its sensitivity to low-level warm and cold advection. Finally, we evaluate 10 state-of-the-art climate models. This paper is organized as follows: datasets and the methodology of the radiative transfer calculations are described in section 2, results are given in section 3, and conclusions are given in section 4.

2. Data and methods

a. Datasets

Cloud observations are taken from the Cloud–Aerosol Lidar with Orthogonal Polarization (CALIOP) instrument onboard the *Cloud–Aerosol Lidar and Infrared Pathfinder Satellite Observations* (*CALIPSO*) satellite. CALIOP is a lidar that measures high vertical resolution profiles of backscatter from which estimates of cloud properties are derived (Winker et al. 2007). Because CALIOP is an active instrument, retrievals are not affected by lack of sunlight or near-surface inversions—two conditions that are common at high latitudes during winter and are problematic for passive satellite retrievals of low clouds. As an example of the challenge of cloud detection with passive instruments over the polar regions, Liu et al. (2004) found that, during polar night, about 40% of all clouds went undetected by the cloud mask algorithm of the Moderate-Resolution Imaging Spectroradiometer (MODIS) used at that time. The algorithm has since been improved (Baum et al. 2012), but detection of low clouds over the polar regions remains a major challenge for passive instruments (Ackerman et al. 2008). Unlike passive instruments, the signal-to-noise ratio of CALIOP is maximized in the absence of sunlight, making it well suited for studying clouds during polar night.

We use the General Circulation Model-Oriented *CALIPSO* Cloud Product (*CALIPSO*-GOCCP) version 2.9 (Chepfer et al. 2010; CALIPSO 2015). *CALIPSO*-GOCCP provides cloud fraction on a 2° longitude, 2° latitude, and 480-m height grid. It also provides low (below 3.2 km), middle (3.2–6.5 km), and high (above 6.5 km) cloud fraction, and estimates for how they are partitioned between liquid and ice. For a given grid box and time interval, cloud fraction is defined as the number of scenes in which a cloud was positively identified divided by the number of scenes in which the lidar was not fully attenuated in the grid box. The lidar beam becomes fully attenuated at an optical depth of ~3 (Winker et al. 2007), so CALIOP often does not measure the bottom portion of low clouds (Cesana et al. 2016). The vertical resolution of CALIOP is 30 m below 8 km and 60 m above 8 km, with a total of 583 vertical levels. Using the relatively coarse GOCCP vertical grid, which has only 40 levels, significantly increases the signal-to-noise ratio and provides a grid that is better for comparison with global climate models (Chepfer et al. 2010).

We also use satellite-based observations of sea ice concentration from the National Oceanic and Atmospheric Administration (NOAA)/National Snow and Ice Data Center (NSIDC) Climate Data Record of Passive Microwave Sea Ice Concentration dataset (Peng et al. 2013; NOAA/NSIDC 2015), and cloud liquid water path from the Multi-Sensor Advanced Climatology of Liquid Water Path (MAC-LWP) dataset (Elsaesser et al. 2016, manuscript submitted to *J. Climate*). Cloud liquid water path is defined as the total mass of cloud liquid water above a unit area of Earth's surface. The latitude of the sea ice edge, which we define as the northernmost point at which the sea ice concentration is 0.35, is computed from the sea ice data. Our main conclusions are not sensitive to choosing a threshold of 0.50 or 0.25 for this definition. We also use temperature, specific humidity, and wind fields from the European Center for Medium-Range Weather Forecasts interim reanalysis (ERA-Interim; Dee et al. 2011; ECMWF 2015). Boundary layer fields in reanalysis products are poorly constrained by observations over the Southern Ocean, and should be interpreted with caution. However, ERA-Interim is consistently ranked among the most reliable reanalysis products in the high southern latitudes (e.g., Bromwich et al. 2011; Bracegirdle and Marshall 2012; Jones et al. 2016).

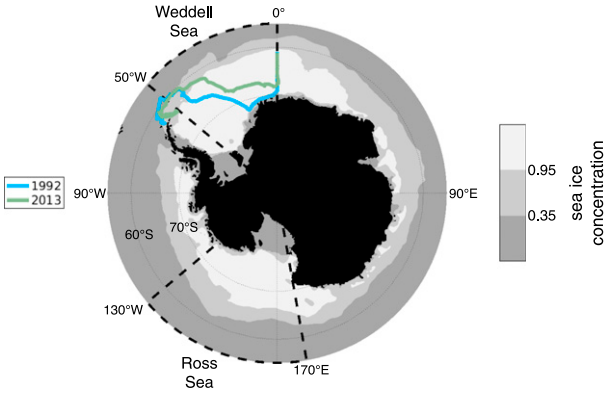

FIG. 1. Map of Antarctica and the Southern Ocean showing average sea ice concentration during July from 2006 to 2014 from satellite observations. Two contours of sea ice concentration are shown: 0.35, which we use as a metric for the sea ice edge, and 0.95. Boundaries for the Weddell (50°W–0°) and Ross (130°W–170°E) Seas are shown in the black dashed lines, and tracks for the cruises to the Weddell Sea are shown as colored lines. The cruises started near 0° longitude and finished near the Antarctic Peninsula.

All satellite and reanalysis data are analyzed on either monthly- or daily-mean time scales during the months of June, July, and August (JJA) from 2006 through 2014. ERA-Interim reanalysis data are available on monthly-mean and instantaneous 6-hourly time resolutions, and daily means are computed from the instantaneous 6-hourly data. Monthly-mean fields are analyzed unless stated otherwise.

Additionally, we use ship-based observations of air temperature and wind speed from soundings, and cloud-base height measured by a ceilometer. Measurements were made on two cruises that traversed the Weddell Sea during June–August 2013 and May–August 1992 (König-Langlo et al. 2006; König-Langlo 2005, 2013). The cruise tracks are shown in Fig. 1. On the 2013 cruise, soundings were launched once per day and have a vertical resolution of about 30 m in the lower troposphere, whereas on the 1992 cruise soundings were launched four times per day and have a vertical resolution of about 60 m. Sounding data are linearly interpolated to a vertical grid with a spacing of 30 m and 60 m on the 2013 cruise and 1992 cruise, respectively. A total of 57 and 161 soundings were taken poleward of 55°S on the 2013 cruise and 1992 cruise, respectively. Wind speed measurements used Global Positioning System (GPS) technology on the 2013 cruise and the OMEGA radio navigation system on the 1992 cruise. As a result, higher-quality wind speed measurements were made on the 2013 cruise (König-Langlo et al. 2006). Measurements of cloud-base height were made on the 1992 cruise but not the 2013 cruise. These ship-based observations complement the satellite observations because the soundings can resolve the vertical structure of the boundary layer and the ceilometer measurements can reliably detect the cloud-base height. The main weakness of the ship-based observations is that measurements are sparse.

Finally, we use output from 10 global climate models that participated in phase 5 of the Coupled Model Intercomparison Project (CMIP5) (Taylor et al. 2012), including output from the *CALIPSO* simulator (Chepfer et al. 2008). Models in fully coupled and atmosphere-only configurations are evaluated, and the first ensemble member for each model is used.

b. *Radiative transfer modeling*

One goal of this study is to quantify the downward flux of LW radiation at the ocean surface, which we call "surface $LW_{\downarrow}$," and its dependence on low-cloud cover. Because direct observations of surface $LW_{\downarrow}$ are not available, we compute it using a radiative transfer model. The advantage of using a radiative transfer model compared to using reanalysis data is that we are able to vary low clouds while holding middle- and high-cloud cover fixed to zero. This method isolates the contribution to surface $LW_{\downarrow}$ made by low clouds.

We use the Rapid and Accurate Radiative Transfer Model for Global Climate Models (RRTM-GCM; Mlawer et al. 1997; Clough et al. 2005; Iacono et al. 2008). This model is one-dimensional and takes vertical profiles of temperature, humidity, cloud liquid, and ice water content as inputs and computes surface $LW_{\downarrow}$. The temperature and humidity profiles are taken from the ERA-Interim reanalysis, and for each profile the surface $LW_{\downarrow}$ is computed with a clear sky and with low cloud completely obscuring the sky. We refer to these values as $LW_{\downarrow,\mathrm{clear}}$ and $LW_{\downarrow,\mathrm{overcast}}$, respectively. A best estimate for the true value of the flux of downward LW radiation at the surface, which we call $LW_{\downarrow,\mathrm{all\text{-}sky}}$, is also computed:

$$LW_{\downarrow,\mathrm{all\text{-}sky}} = LW_{\downarrow,\mathrm{clear}}(1 - \mathrm{LCF}) + LW_{\downarrow,\mathrm{overcast}}\mathrm{LCF},$$

where LCF is the low-cloud fraction observed by *CALIPSO*. Daily-mean data are used because they have the shortest time resolution for which *CALIPSO*-GOCCP cloud observations are available.

The radiative transfer calculations are done only for regions of open water near the sea ice edge. We focus on scenes between 1° and 3° equatorward of the ice edge, where the sea ice concentration is approximately zero. This restriction is made because microwave, satellite-based retrievals of cloud liquid water path are not available over sea ice. Although the domain is restricted to open water scenes only, the surface heat budget over open water is of interest because extreme air–sea heat fluxes can occur there (e.g., Papritz et al. 2015).

TABLE 1. Summary of observations used to guide the radiative transfer calculations. (top) Cloud fraction partitioned by cloud height and cloud thermodynamic phase from *CALIPSO*-GOCCP observations. (middle) Summary of the distribution of cloud liquid water path from MAC-LWP observations. Cloud phase and liquid water path are from satellite observations taken during JJA from 2006 to 2014 over open water near the sea ice edge in the Weddell Sea. (bottom) Cloud-base height measurements from a cloud ceilometer onboard the 1992 cruise. Statistics of cloud-base height are shown for all scenes in which a cloud with a base below 1500 m was detected and surface observers reported open water or open pack ice near the ship. The probability density function shown in parentheses was computed by dividing the probability of each bin by the width of the bin.

Cloud phase

Level	Total cloud fraction	Liquid cloud fraction	Ice cloud fraction	Unclassified cloud fraction
High	0.29	0	0.28	0.02
Middle	0.27	0.09	0.16	0.04
Low	0.69	0.50	0.05	0.14

Liquid water path

Percentile	5	25	50	75	95
Liquid water path ($g\,m^{-2}$)	43.1	54.1	61.4	70.1	79.1

Cloud-base height

Height range (m)	0–50	50–100	100–200	200–300	300–600	600–1000	1000–1500
Counts [probability density $\times 10^{-2}$; (m^{-1})]	12 (0.10)	11 (0.09)	22 (0.09)	36 (0.15)	58 (0.08)	67 (0.07)	34 (0.03)

In the radiative transfer calculations, several assumptions about low clouds are made that are based on observations presented in Table 1. First, low clouds are assumed to consist entirely of supercooled liquid. *CALIPSO*-GOCCP observations of cloud fraction partitioned by phase are presented in Table 1 and show that low clouds over the Southern Ocean are frequently composed of liquid, consistent with previous studies (Hu et al. 2010; Morrison et al. 2011). Cesana et al. (2016) suggest that low clouds with unclassified phase in the *CALIPSO*-GOCCP dataset are mostly mixed-phase clouds. Even so, at least three-quarters of the low clouds detected by *CALIPSO* are liquid (low-cloud fraction is 0.50 for liquid clouds and 0.69 for all phases). Second, all cloud liquid water is assumed to reside in the lowest 3.2 km of the atmosphere. Under this assumption the column-integrated cloud liquid water path is equal to the total liquid water contained in low clouds. This assumption is justified by the *CALIPSO* phase observations (Table 1), which show that liquid clouds are usually found at low levels. Third, the liquid water path is assumed to be $60\,g\,m^{-2}$, which is near the median of satellite observations (Table 1). Fourth, the heights of low-cloud base and top are set to 500 m and 1000 m, respectively. The cloud-base height value comes from measurements from the 1992 cruise taken when surface observers reported open water or open pack ice near the ship (Table 1). During this cruise, observed cloud-base height was distributed nearly uniformly between the surface and 1000 m. Fifth, low clouds are assumed to have a droplet effective radius of 16 μm, which is close to the observed wintertime mean over the Southern Ocean (McCoy et al. 2014, their Fig. 9).

Our results are insensitive to modest changes in these five assumptions about low-cloud properties. To test the sensitivity of the radiative transfer calculations to the assumptions about low-cloud properties, runs were performed with cloud-base height set to 0 and 1000 m, with liquid water path halved to $30\,g\,m^{-2}$, and with cloud effective radius doubled to 32 μm and halved to 8 μm. The results are not sensitive to modest changes in liquid water path because liquid clouds are nearly opaque to LW radiation for liquid water path values greater than $\sim 20\,g\,m^{-2}$ (Hartmann 2016), which is much lower than observed values (Table 1). In fact, each modification of the assumptions resulted in a change in $LW_{\downarrow,overcast}$ of about $7\,W\,m^{-2}$ or less, which is small compared to the contribution to surface $LW_{\downarrow}$ made by low clouds during overcast conditions ($\sim 80\,W\,m^{-2}$; discussed in the results section). In other words, to leading order, low-cloud fraction controls the surface LW radiative effect from low clouds. The model error is less than $1\,W\,m^{-2}$ (Mlawer et al. 1997), which is much smaller than the uncertainty due to the five assumptions made about cloud properties.

3. Results

a. *Satellite observations of sea ice and low cloud over the Southern Ocean*

We start with a brief description of Antarctic sea ice during winter. Figure 1 shows July-average sea ice

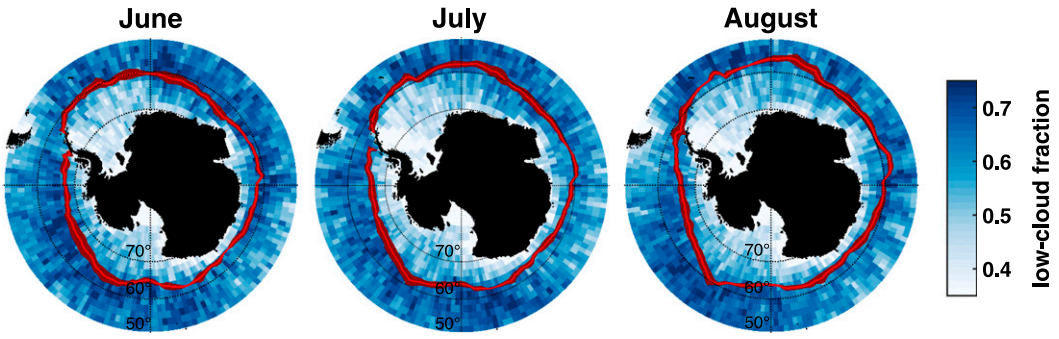

FIG. 2. The 2006–14 winter climatology of low-cloud fraction (color) from *CALIPSO*-GOCCP observations and the position of the sea ice edge. The red line shows the average position of the sea ice edge, and the red shading shows one standard deviation on either side of the mean.

concentration over the Southern Ocean. Two contours of sea ice concentration are shown: 0.35 and 0.95. These contours can be thought of as marking the boundaries between open water, fragmented sea ice, and a sea ice pack that covers the surface nearly completely. Throughout most of the Eastern Hemisphere, sea ice concentration rarely exceeds 0.95. This could be a result of the coastline extending equatorward and forcing the sea ice closer to the Antarctic Circumpolar Current. In regions where the coastline cuts poleward, like the Weddell and Ross Seas, sea ice concentrations greater than 0.95 are much more common. Average sea ice concentrations in June and August are similar in this regard (not shown). Wadhams et al. (1987) describe the winter sea ice pack in the Weddell Sea as observed from a cruise. They found the marginal sea ice zone to be a band of fragmented pancake ice with pockets of exposed seawater. Farther south, they found sea ice organized into vast floes that covered the ocean surface nearly completely. We recommend viewing photographs of these features in Wadhams et al. (1987, their Fig. 12).

Now, consider low-cloud fraction over the Southern Ocean. The winter climatology of low-cloud fraction and the latitude of the sea ice edge are shown in Fig. 2. The interannual standard deviation of the latitude of the sea ice edge ranges between about 0.5° to 1.5° latitude. One standard deviation on either side of the mean position of the sea ice edge is shaded in Fig. 2 to show that the effects of interannual variability of the location of the ice edge are likely small. Throughout the Southern Ocean, cloudier conditions are seen over open water than over sea ice. Near the sea ice edge, low-cloud fraction is about 0.7 over open water and 0.5 over sea ice. The gradient of low-cloud fraction across the sea ice edge is weakest in the southern Indian and western Pacific Oceans (20°–160°E). This weak gradient is likely because the sea ice pack is more fragmented in this region than elsewhere in the Southern Ocean (Fig. 1). In this region, the low-cloud fraction is more variable over sea ice than over open water because gaps in the sea ice pack are found throughout the ice pack, but little sea ice is found equatorward of the sea ice edge. In the Weddell and Ross Seas, where the sea ice pack covers the surface nearly completely, the low-cloud fraction is about 0.4 or less and the gradient in low-cloud fraction across the sea ice edge is sharp.

The relationship between sea ice concentration and low-cloud properties near the sea ice edge is made clearer by stratifying the observations based on distance from the sea ice edge. For each grid point and time (JJA monthly means between 2006 and 2014 are considered), the meridional distance between the grid point and the ice edge is computed. Data are then composited by meridional distance from the ice edge, using a bin width of 0.5° latitude, and averaged. We analyze data from the Weddell and Ross Seas (defined as 50°W–0°E and 130°W–170°E, respectively), two regions where the sea ice pack covers the surface nearly completely and where the sea ice edge is located far offshore (Fig. 1). This procedure was also done on the JJA-mean of each year, and the main conclusions are the same using either monthly or seasonal averages.

Figure 3a shows the vertical profile of mean cloud fraction in the lower troposphere over the Weddell Sea as a function of meridional distance from the sea ice edge, and Fig. 3d is similar but for the Ross Sea. On average, low clouds extend deeper and are more prevalent equatorward of the sea ice edge. The mean low-cloud fraction and sea ice concentration are shown in Figs. 3b and 3e, and the method for deriving the confidence interval for the mean is described in the appendix. The domain can be split into three regions based on sea ice concentration: an ''ice'' zone where sea ice concentration is ~1 that is located poleward of

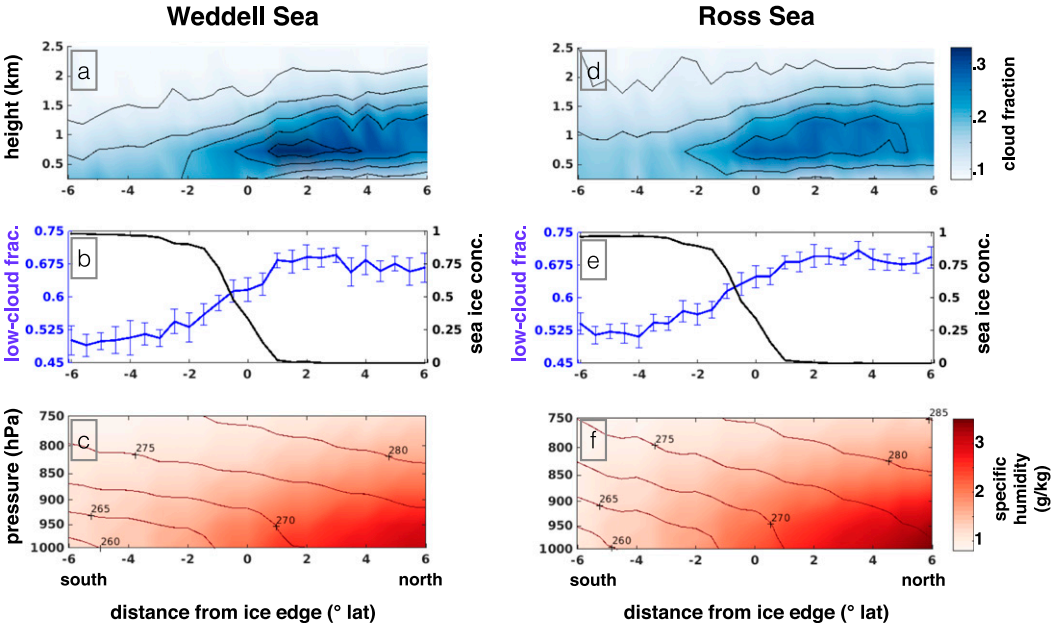

FIG. 3. Wintertime cloud fraction, temperature and humidity in the lower troposphere plotted as a function of meridional distance from the sea ice edge. (a) Vertical profile of mean cloud fraction, (b) mean sea ice concentration and low-cloud fraction, with error bars showing the 95% confidence interval of the mean, and (c) mean potential temperature (contours) and specific humidity (color) over the Weddell Sea. (d)–(f) As in (a)–(c), but for the Ross Sea. Cloud and sea ice fields come from satellite observations, and temperature and humidity come from ERA-Interim reanalysis data. The boundaries for the Weddell Sea and Ross Sea are shown in Fig. 1.

2° south of the ice edge, an ''open water'' zone where sea ice concentration is ~0 that is located equatorward of 1° north of the ice edge, and a ''transition'' zone between. Within the ice zone the mean low-cloud fraction is nearly uniform at around 0.5, and within the open water zone the mean low-cloud fraction is nearly uniform at around 0.7. The mean low-cloud fraction is significantly larger in the open water zone than the ice zone. From south to north across the transition zone, the low-cloud fraction increases smoothly as sea ice concentration decreases.

Figures 3c and 3f show vertical profiles of mean potential temperature and specific humidity from reanalysis data as a function of meridional distance from the ice edge. In current reanalysis data, the surface heat budget and the atmospheric boundary layer over the Southern Ocean are poorly constrained by observations, and therefore these data should be interpreted with caution. Nevertheless, the data suggest several differences between the boundary layer over sea ice and over open water. The lower troposphere is more stable over sea ice than over open water, as can be seen by the vertical spacing in the potential temperature contours. Over open water, near-surface temperatures are close to the freezing temperature of seawater, and across the sea ice edge, near-surface temperatures drop rapidly. Boundary layer specific humidity values are also nearly a factor of 2 larger over open water than over sea ice.

b. *Boundary layer structure from ship-based observations*

Soundings resolve the vertical structure of the boundary layer and provide further insight into the physical processes at work. In this section, sounding data are represented by probability distributions. For each height measured by the soundings, the probability distributions are computed by binning the data, computing the number of observations in each bin, and normalizing by the total number of soundings. Data are composited into measurements made between 55° and 65°S and poleward of 65°S. Because the sea ice edge is typically located between 60° and 65°S in the Weddell Sea during winter, it is likely that most of the soundings poleward of 65°S were taken over consolidated pack ice. Meanwhile, soundings between 55° and 65°S are likely a mixture of some taken over consolidated pack ice and some taken where open water was exposed to the atmosphere.

Figure 4 shows the probability distribution of temperature at each height between 10 and 1500 m. The 2013 and 1992 cruises are shown separately in Figs. 4a,b and 4c,d, respectively, because the cruises used

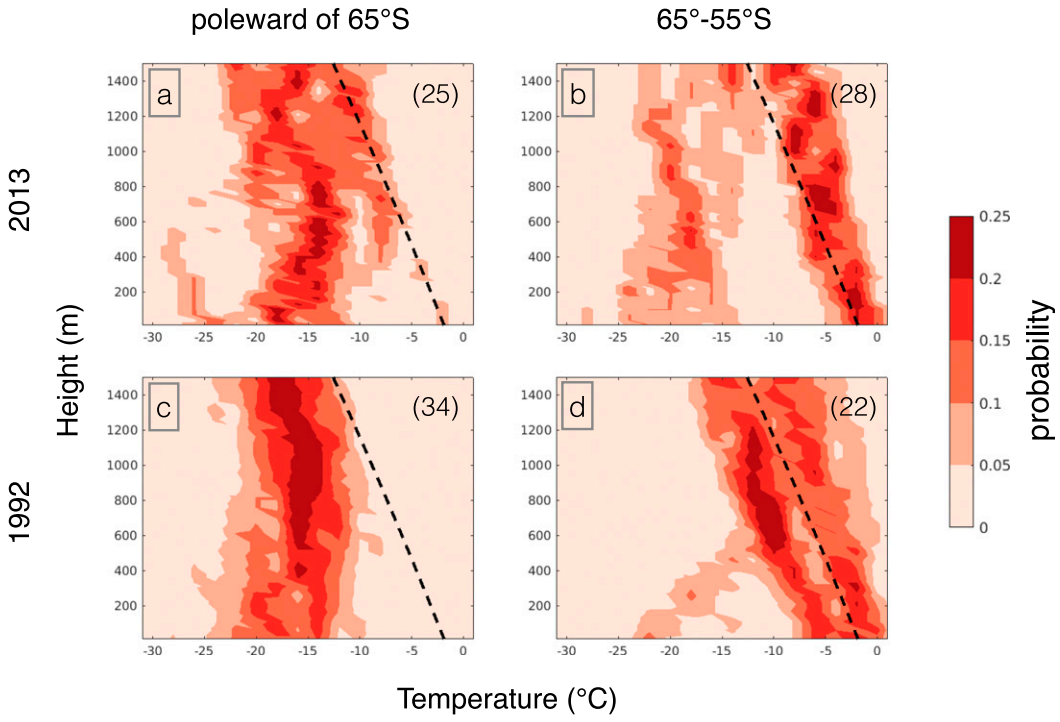

FIG. 4. Temperature profile of the lower troposphere over the Weddell Sea from soundings. For each height, color shows the probability density function of air temperature. Data are composited into soundings taken poleward of 65°S and between 55° and 65°S. The number of days in which soundings were collected is shown in the top-right corner of each panel. (a),(b) The 2013 cruise and (c),(d) the 1992 cruise. Bins of width 2°C are used in the calculation. The black dashed line shows a profile with a surface temperature of −1.8°C, which is about the freezing temperature of seawater in the Southern Ocean, and a moist adiabatic lapse rate. Note that two boundary layer regimes are seen: a warm mode with near-surface temperatures close to the freezing temperature of seawater and with a most adiabatic lapse rate, and a cold mode with near-surface temperatures from −15° to −25°C and with a low-level inversion.

different sounding technologies (König-Langlo et al. 2006) and had different times between successive launches. Two boundary layer regimes are seen: a warm and a cold mode. The warm mode is characterized by having near-surface temperatures close to the freezing temperature of seawater and by a moist adiabatic lapse rate above. In this regime the boundary layer is well mixed and moist. The cold mode is characterized by typical near-surface temperatures of about −15° to −25°C and by a low-level inversion. Poleward of 65°S, the cold mode dominates (Figs. 4b,d). Between 55° and 65°S, both the warm and the cold modes are seen, albeit with different likelihoods between the two cruises (Figs. 4a,c). Differences in the relative occurrence of the warm and cold mode in the 55°–65°S composite between the two cruises could be a result of different weather events. The latitudinal distribution of the warm and cold modes suggests that the cold mode forms over consolidated pack ice, and the warm mode forms over open ocean or gaps in the sea ice.

The soundings also measured wind speed, and this is shown in Fig. 5. The probability distribution of wind speed as a function of height is shown for all soundings taken poleward of 55°S. Sounding data are not composited by latitude here, but doing so results in composites that resemble Fig. 5 but are noisier (not shown). The soundings reveal that wind speeds of $10\,m\,s^{-1}$ or more are common at heights of 200–600 m. For both cruises, the average wind speed between 200–600 m is $10\,m\,s^{-1}$ or more for 60%–70% of the soundings. For the 2013 cruise, the strong low-level winds are often associated with a low-level jet. On this cruise, the modal value of wind speed is ~12–15 $m\,s^{-1}$ at heights of 200–400 m and decreases with height to ~8 $m\,s^{-1}$ at heights of 800–1000 m (Fig. 5a). Data from both cruises show that strong low-level winds are common during winter.

Low-level jets are of interest because they indicate the presence of a stable boundary layer. Low-level jets exist at the top of stable boundary layers and, at least in temperate latitudes, are initiated when the boundary layer transitions from convective to stable. During this transition, the sudden shoaling of the boundary layer causes a reduction in drag from turbulent momentum

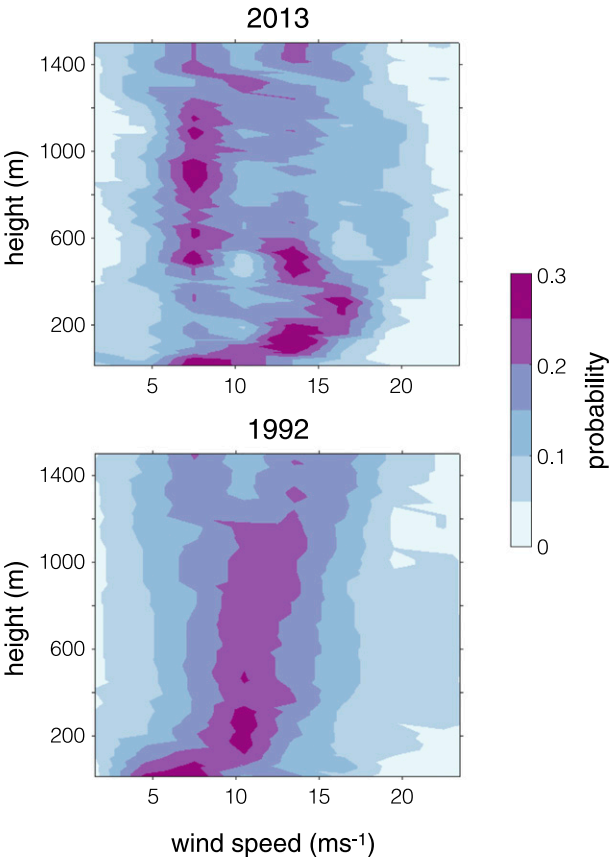

FIG. 5. Vertical profile of wind speed from soundings in the Weddell Sea poleward of 55°S, from the (top) 2013 and (bottom) 1992 cruise. For each height, color shows the probability density function of wind speed. Bins of width 3 m s^{-1} are used in the calculation. Data were collected over 53 days on both cruises. Note that wind speeds of 10 m s^{-1} or more are common at heights between 200 and 600 m, and that the signature of a low-level jet can be seen in the measurements from the 2013 cruise.

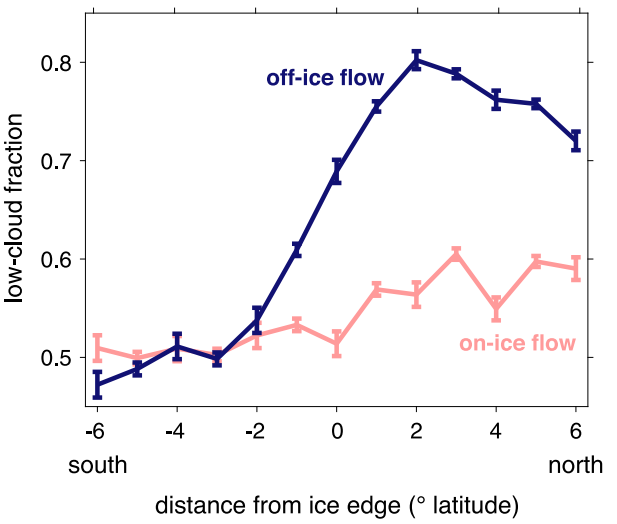

FIG. 6. Mean low-cloud fraction observed by *CALIPSO* as a function of meridional distance from the sea ice edge, and its dependence on low-level warm or cold advection. Observations are composited into periods of poleward, on-ice flow at low levels ($v_{\text{ice edge}} < -0.5\sigma \approx -3$ m s^{-1}, where σ is the standard deviation of $v_{\text{ice edge}}$) and periods of equatorward, off-ice flow at low-levels ($v_{\text{ice edge}} > 0.5\sigma \approx 3$ m s^{-1}). Averages are computed using daily-mean data, and error bars show the 95% confidence interval of the mean. Over open ocean, cloudier conditions are seen during periods of off-ice advection. Over sea ice, low-cloud fraction is similar during periods of on-ice and off-ice advection.

flux, and therefore a sudden increase in wind speed, at heights above the stable boundary layer but below the top of the former convective boundary layer. The stable boundary layer limits drag on the winds above and allows the jet to persist and follow an inertial oscillation (Blackadar 1957; Thorpe and Guymer 1977). The mechanisms that initiate low-level jets over Antarctic sea ice during winter are not fully understood. One possible mechanism is warm advection from open water to sea ice covered regions, which temporarily deepens the boundary layer and then allows a new jet to form when the boundary layer collapses to a stable profile (Andreas et al. 2000). Another possible mechanism is motions arising from baroclinic instability associated with the thermal contrast between sea ice and open ocean.

We emphasize that a weakness of this study is the short time span of sounding data. Soundings were taken over a total of 50 days between 55° and 65°S and 59 days poleward of 65°S. Despite this drawback, the main conclusions are robust: in both cruises, a warm and a cold boundary layer regime are seen, and low-level wind speeds in excess of 10 m s^{-1} are common.

c. *Advection across the sea ice edge*

How do clouds respond when cold air is advected equatorward, across the sea ice edge, and vice versa? We start with an investigation of low-cloud fraction and its sensitivity to advection across the sea ice edge. Cold air outbreaks, in which air is advected from a cold land or ice surface to a warmer ocean, are known to cause the development of low clouds (e.g., Walter 1980; Liu et al. 2006). When the cold air mass is heated from below by the warm ocean surface, convection occurs and low clouds form. Once formed, low clouds are maintained by radiative cooling at cloud top, radiative heating at cloud base, and the moisture source of the ocean.

Figure 6 shows the mean low-cloud fraction as a function of meridional distance from the sea ice edge, stratified by low-level advection across the sea ice edge. As a metric for low-level advection across the sea ice edge, the meridional wind at 1000 hPa is linearly interpolated to the latitude of the sea ice edge. We refer to this value as $v_{\text{ice edge}}$. Data are composited into scenes in

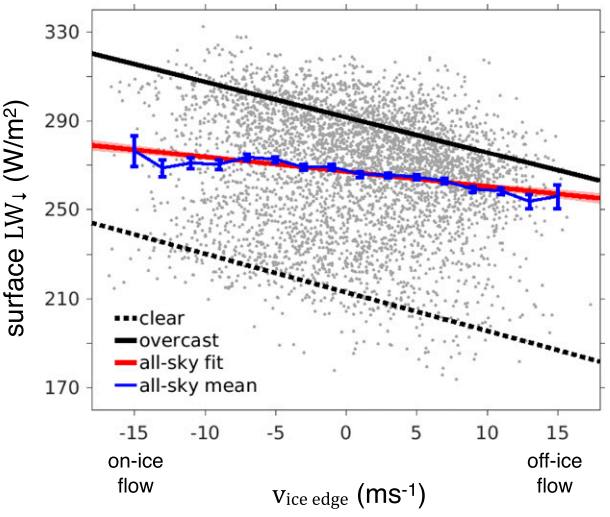

FIG. 7. Surface $LW_{\downarrow}$ over open water near the sea ice edge plotted as a function of near-surface meridional wind at the sea ice edge ($v_{\text{ice edge}}$). The dots show individual $LW_{\downarrow,\text{all-sky}}$ values, and the blue line shows $LW_{\downarrow,\text{all-sky}}$ binned by $v_{\text{ice edge}}$ and averaged. Error bars on the blue line are the 95% confidence interval of the mean. The red, solid black, and dashed black lines show linear regressions of $LW_{\downarrow,\text{all-sky}}$, $LW_{\downarrow,\text{overcast}}$, and $LW_{\downarrow,\text{clear}}$ on $v_{\text{ice edge}}$, respectively. The red shading is the 95% confidence interval for the regression slope of $LW_{\downarrow,\text{all-sky}}$. Note that surface LW cloud radiative effect, seen in the figure as the difference between $LW_{\downarrow,\text{all-sky}}$ and $LW_{\downarrow,\text{clear}}$, increases with $v_{\text{ice edge}}$. As a result, surface LW cloud radiative effect is largest during periods of strong off-ice flow.

which $v_{\text{ice edge}}$ is less than $-0.5\sigma \approx -3\,\text{m s}^{-1}$ and greater than $0.5\sigma \approx 3\,\text{m s}^{-1}$, where σ is the standard deviation of $v_{\text{ice edge}}$. These composites correspond to on-ice flow and off-ice flow, respectively. These composites are made using daily-mean data over the Weddell Sea. The mean low-cloud fraction equatorward of the sea ice edge is significantly larger during periods of off-ice flow than periods of on-ice flow. The peak in low-cloud fraction during periods of off-ice flow is located at about 2° equatorward of the ice edge, suggesting that low clouds formed by cold advection can persist well away from the sea ice edge. The fact that the peak in low-cloud fraction is about 2° latitude equatorward of the sea ice edge may be a result of the predominant low-cloud type transitioning from roll clouds near the sea ice edge to cellular convection downstream (Walter 1980). This hypothesis is also consistent with the composites in Figs. 3a and 3d, which show that, near the sea ice edge, the low-cloud layer deepens toward the equator. Finally, for latitudes 2° south of the ice edge and poleward, where sea ice covers the surface nearly completely (Fig. 3b), there is either no significant difference, or a very small difference, in low-cloud fraction between the on-ice flow and off-ice flow composites. This result suggests that low clouds over open water are coupled to the surface and require the moisture source of the open ocean to exist, and therefore dissipate when separated from open water.

d. *Impact of low-level advection on the surface heat budget*

We have seen evidence of a warm and a cold boundary layer regime, and that cold, low-level advection off of the sea ice pack causes low clouds to form over open water. How do low-level advection and the resulting boundary layer and low-cloud changes impact the surface heat budget? To address this question we use a radiative transfer model to compute surface $LW_{\downarrow}$ over open water near the sea ice edge and to estimate the contribution made by low clouds. The Weddell Sea is again used as the region of study. Recall that estimates of surface $LW_{\downarrow}$ are computed for a clear sky, with low cloud completely covering the sky, and using low-cloud fraction observed by *CALIPSO*. These values will be called $LW_{\downarrow,\text{clear}}$, $LW_{\downarrow,\text{overcast}}$, and $LW_{\downarrow,\text{all-sky}}$ respectively. The $LW_{\downarrow,\text{all-sky}}$ values are the best estimate for the real world, while the $LW_{\downarrow,\text{clear}}$ and $LW_{\downarrow,\text{overcast}}$ values help with interpretation. Also, recall that there are no middle or high clouds in these calculations, so the radiative effects of low clouds are isolated here.

First, consider the average values of surface $LW_{\downarrow}$. The average values of $LW_{\downarrow,\text{clear}}$ and $LW_{\downarrow,\text{overcast}}$ are about 210 and 290 W m^{-2}, respectively. In other words, if a point at the ocean surface were located under a clear sky, and a low-cloud passed overhead, then the downward flux of LW radiation would suddenly increase by about 80 W m^{-2}, a 40% increase from the clear-sky value. The average value of $LW_{\downarrow,\text{all-sky}}$ is around 270 W m^{-2}. The surface LW cloud radiative effect, defined as $LW_{\downarrow,\text{all-sky}} - LW_{\downarrow,\text{clear}}$, is about 50–60 W m^{-2}. During winter, low clouds warm the ocean surface by about 50–60 W m^{-2} on average.

Furthermore, surface $LW_{\downarrow}$ depends on the strength of warm or cold advection at low levels. In the calculations of $LW_{\downarrow,\text{clear}}$ and $LW_{\downarrow,\text{overcast}}$, temperature and specific humidity are varied but low-cloud fraction is held fixed, and therefore the surface LW cloud radiative effect is nearly constant. In the calculation of $LW_{\downarrow,\text{all-sky}}$, temperature, humidity, and low-cloud fraction are all varied. Thus, by comparing data from the $LW_{\downarrow,\text{all-sky}}$, $LW_{\downarrow,\text{clear}}$, and $LW_{\downarrow,\text{overcast}}$ calculations, the sensitivity of surface $LW_{\downarrow}$ to low-cloud variations can be separated from the effects of temperature and humidity variations.

Figure 7 shows surface $LW_{\downarrow}$ plotted as a function of $v_{\text{ice edge}}$. In the $LW_{\downarrow,\text{clear}}$ and $LW_{\downarrow,\text{overcast}}$ calculations, where low-cloud fraction is held fixed, the data are anticorrelated with $v_{\text{ice edge}}$ ($r = -0.61$ and $r = -0.64$, respectively). This happens because air masses that form over the sea ice pack are cold and have low specific

humidity, and these features of the air cause it to radiate relatively weakly to the surface when advected over open water (when low-cloud fraction is held fixed). However, in the $LW_{\downarrow,\text{all-sky}}$ calculation, where low-cloud fraction is varied according to *CALIPSO* observations, data are weakly anticorrelated with $v_{\text{ice edge}}$ (scatterplot in Fig. 7). When the $LW_{\downarrow,\text{all-sky}}$ data are binned by $v_{\text{ice edge}}$ and averaged, the result agrees well with a linear regression (cf. the blue and red lines in Fig. 7). Because cold advection causes cloudy conditions, $LW_{\downarrow,\text{all-sky}}$ data approach the $LW_{\downarrow,\text{overcast}}$ regression line for large positive values of $v_{\text{ice edge}}$. The surface LW cloud radiative effect, seen in Fig. 7 by the difference between $LW_{\downarrow,\text{all-sky}}$ and $LW_{\downarrow,\text{clear}}$, increases by $1.1 \pm 0.1\,\text{W m}^{-2}$ per $1\,\text{m s}^{-1}$ increase in $v_{\text{ice edge}}$. Put another way, typical values of the average surface LW cloud radiative effect, estimated by the regression, range from 43 to $65\,\text{W m}^{-2}$ for $v_{\text{ice edge}} = -10\,\text{m s}^{-1}$ to $v_{\text{ice edge}} = 10\,\text{m s}^{-1}$, respectively. As a result, the regression coefficient of $LW_{\downarrow,\text{all-sky}}$ on $v_{\text{ice edge}}$ ($-0.7 \pm 0.1\,\text{W m}^{-2}$ per $1\,\text{m s}^{-1}$ increase in $v_{\text{ice edge}}$) is significantly smaller in magnitude than the regression coefficients of $LW_{\downarrow,\text{clear}}$ and $LW_{\downarrow,\text{overcast}}$ (cf. slopes in Fig. 7). Therefore, when low-cloud fraction, temperature, and humidity are all allowed to vary, as they are in the real world, then surface $LW_{\downarrow}$ is much less sensitive to warm or cold advection than when low-cloud fraction is held fixed. Low clouds warm the surface most strongly during cold advection events, and therefore act to reduce the sensitivity of surface $LW_{\downarrow}$ to cold advection.

We emphasize that these calculations are only able to capture one term of the surface heat budget: surface $LW_{\downarrow}$. Surface turbulent heat fluxes are likely very important as well. Over open water in the Southern Ocean during winter, average values of surface turbulent fluxes of sensible and latent heat are around 30 and $50\,\text{W m}^{-2}$ respectively—on the order of the average surface LW cloud radiative effect—but surface turbulent heat fluxes can be several hundred watts per square meter during extreme cold air outbreaks (Papritz et al. 2015). These turbulent heat flux values come from reanalysis data, and should therefore be interpreted with caution. Our work is progress toward constraining the surface heat budget of the Southern Ocean, but a complete understanding also requires knowledge of the surface turbulent heat flux.

e. Evaluation of global climate models

We have seen that the surface LW cloud radiative effect from low clouds is about 50–$60\,\text{W m}^{-2}$ on average. Therefore, low-cloud biases in global climate models (GCMs) have the potential to significantly bias the modeled surface heat budget. Accurate representation of marine boundary layer clouds and their radiative effects are a major challenge for GCMs (Dufresne and Bony 2008; Trenberth and Fasullo 2010), and low clouds are especially poorly represented in GCMs during polar night (Karlsson and Svensson 2011). Here we evaluate the climatology of low-cloud fraction near the sea ice edge in 10 GCMs. Low-cloud fraction in the models is computed by a *CALIPSO* simulator that estimates what *CALIPSO* would observe if it were flying above the atmosphere in the model. Both fully coupled and atmosphere-only (AMIP) configurations are analyzed between 1990 and 2004 (Taylor et al. 2012; Gates 1992). Fully coupled models have prescribed atmospheric greenhouse gas concentrations from observations, while atmosphere-only models have prescribed sea surface temperature and sea ice concentration from observations. Most importantly, interactions between the ocean, sea ice, low clouds, and the atmospheric boundary layer are active in fully coupled configuration and are suppressed in atmosphere-only configuration. Model climatologies are compared to the observed climatology between 2006 and 2014.

Figure 8 shows the July-mean low-cloud fraction observed by *CALIPSO* and simulated by six GCMs that have output from both atmosphere-only and fully coupled configuration. Model behavior is quite diverse. Starting with the atmosphere-only runs, HadGEM2, MIROC5, and MRI-CGCM3 have cloudier conditions over open water than over sea ice. However, the gradient in low-cloud fraction across the sea ice edge is weak in MIROC5. The IPSL models and MRI-CGCM3 significantly underestimate low-cloud cover over open water. Compared to the atmosphere-only runs, models in fully coupled configuration generally have similar low-cloud fractions, and the MIROC5 and MPI-ESM-LR models have a sea ice edge that is located too close to the coastline. The models do not capture the weaker low-cloud fraction gradient across the sea ice edge in the Eastern Hemisphere that is seen in observations (Fig. 2). Other than that, the modeled low-cloud fraction does not have any systematic geographic bias.

Model bias in low-cloud fraction is quantified and shown in Fig. 9. As a metric for the low-cloud fraction near the sea ice edge, the mean low-cloud fraction is computed over open water and sea ice, again defined as 1°–3° equatorward and 2°–4° poleward of the ice edge, respectively. These will henceforth be referred to as $LCF_{\text{open water}}$ and $LCF_{\text{sea ice}}$. One common feature between models is a bias of too little low-cloud fraction over open water, consistent with previous work (e.g., Zhang et al. 2005). In fact, over open water, 9 out of 10 models underestimate low-cloud fraction, one model (GFDL-CM3) agrees with observations at 95% confidence,

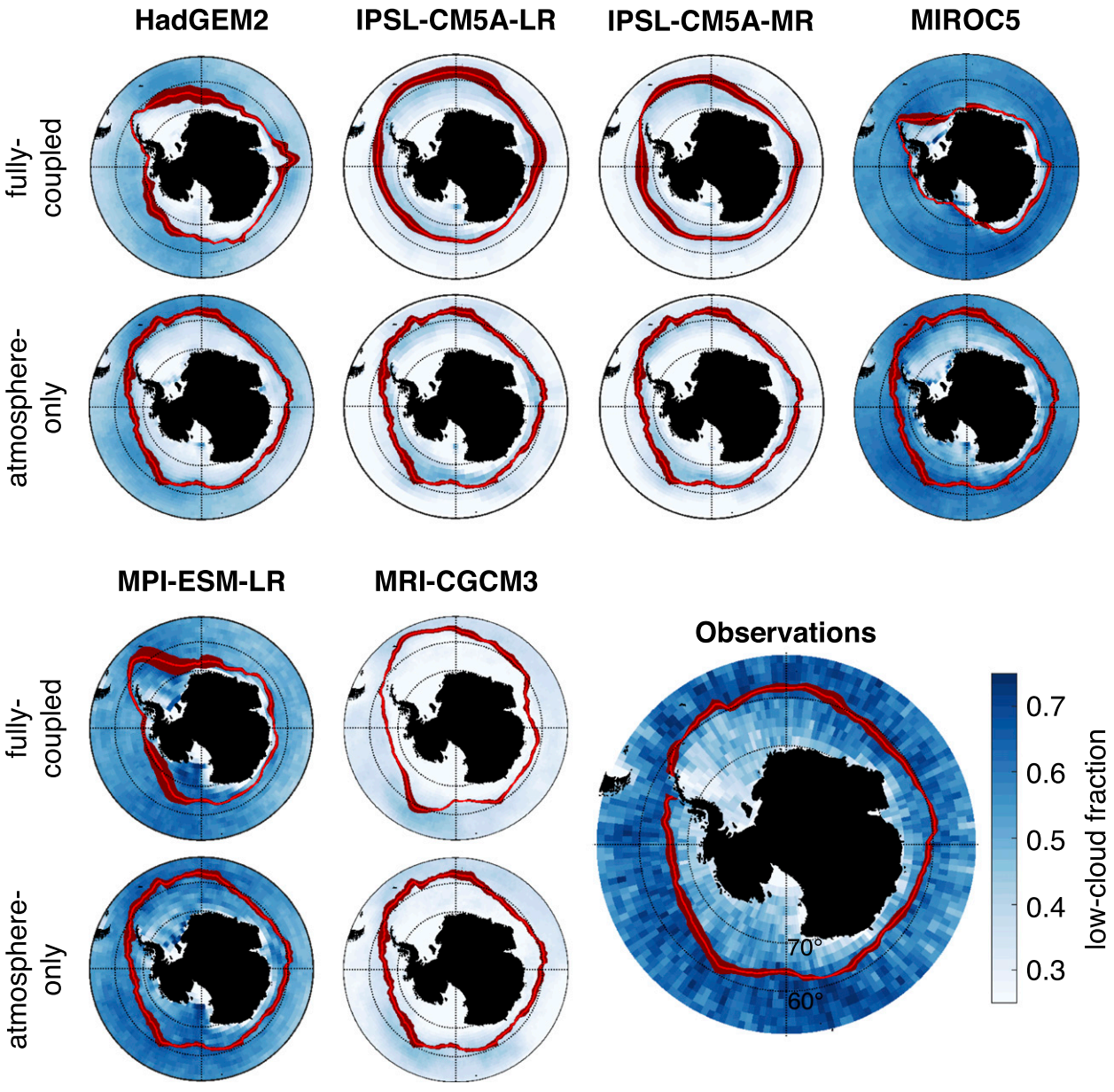

FIG. 8. July-mean low-cloud fraction and latitude of the sea ice edge in climate models and observations. Low-cloud fraction is shown in blue, and the sea ice edge is shown in red (the red line shows the mean, and red shading shows one standard deviation on either side of the mean). Each model is shown with output from fully coupled and atmosphere-only configuration. Low-cloud fraction in the models was computed by a *CALIPSO* simulator, and observations are from *CALIPSO*-GOCCP.

and no models overestimate low-cloud fraction. This can be seen by noting that $LCF_{open\ water}$ for all of the models appears to the left of the observations in Fig. 9a. The magnitude of the largest model bias is about 0.35 (IPSL models), meaning that low-cloud fraction in these models is roughly half of the observed value. Model bias in $LCF_{sea\ ice}$ is more diverse and ranges from +0.15 to −0.26. However, out of the eight fully coupled models, all but one model underestimate $LCF_{sea\ ice}$, one model agrees with observations (MPI-ESM-LR), and no models overestimate $LCF_{sea\ ice}$. This can be seen by noting that all but one of the fully coupled models are below the observations in Fig. 9a. Again, models that underestimate low-cloud fraction the most have low-cloud fractions that are roughly half of the observed value. Most models underestimate low-cloud fraction over open water and over sea ice.

Having established the mean low-cloud fraction bias in the models, we now examine the difference of

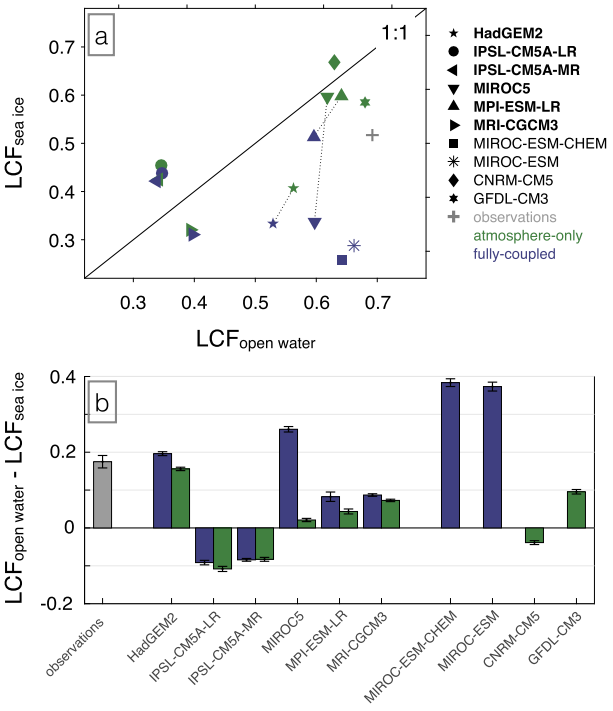

FIG. 9. Evaluation of wintertime low-cloud fraction near the sea ice edge in climate models. (a) *CALIPSO* observed and simulated mean low-cloud fraction over open water (1°–3° equatorward of the sea ice edge) and sea ice (2°–4° poleward of the sea ice edge). The gray plus sign shows the 95% confidence interval for the observed value. Models in both atmosphere-only and fully coupled configurations are shown. Six models have both atmosphere-only and fully coupled output, and these models are labeled with bold text in the legend. For these models, the atmosphere-only and fully coupled data points are connected by a dashed line, but for some models the difference is small and the dashed line is not visible. Note that all but one model (GFDL-CM3) underestimate low-cloud fraction over open water, and all but one fully coupled model (MPI-ESM-LR) underestimate low-cloud fraction over sea ice. (b) Difference between mean low-cloud fraction over open water and over sea ice near the sea ice edge. Error bars show the 95% confidence interval.

low-cloud fraction between the open water and sea ice regions, which is shown in Fig. 9b. Seven out of 10 models have significantly cloudier conditions over open water than over sea ice. Although most models capture the correct sign of $\mathrm{LCF}_{\text{open water}} - \mathrm{LCF}_{\text{sea ice}}$, the magnitude varies between 0.38 in the MIROC-ESM and MIROC-ESM-CHEM models and −0.11 in the IPSL models, while the observed value is $\mathrm{LCF}_{\text{open water}} - \mathrm{LCF}_{\text{sea ice}} = 0.17 \pm 0.01$.

Finally, we consider how low clouds change with model resolution and configuration. Models that have both atmosphere-only and fully coupled output provide an opportunity to compare low clouds when the ocean and sea ice are prescribed and when they are interactive. Of these six models that have both atmosphere-only and fully coupled output, three have little or no difference between low-cloud fraction in fully coupled and atmosphere-only configuration (IPSL-CM5A-LR, IPSL-CM5A-MR, and MRI-CGCM3). However, these models also underestimate low-cloud fraction the most (Figs. 8 and 9a). The MIROC5 and MPI-ESM-LR models have more realistic values of $\mathrm{LCF}_{\text{open water}} - \mathrm{LCF}_{\text{sea ice}}$ in the atmosphere-only configuration than in the fully coupled configuration (Fig. 9b), but this may be due to the fact that the sea ice edge in these models is much closer to shore, and therefore more exposed to cold continental air, in fully coupled configuration (Fig. 8). Finally, the IPSL models make for an interesting comparison because they differ only in resolution: IPSL-CM5A-LR and IPSL-CM5A-MR have horizontal resolutions of $1.9° \times 3.75°$ and $1.25° \times 2.5°$, respectively. In this model, finer resolution does not improve the low-cloud bias.

4. Summary and conclusions

During austral winter, active satellite retrievals from *CALIPSO* and ship-based measurements show a strong contrast in low-cloud fraction and boundary layer structure over Antarctic sea ice and the adjacent open ocean. Low-cloud fraction is roughly 0.7 over open water and 0.4–0.5 over sea ice, and the low-cloud layer is much deeper over open water. The boundary layer is cold, stable, dry and clear over consolidated sea ice and warm, moist, cloudy, and well mixed over open water. At heights of 200–600 m, wind speeds in excess of $10\,\mathrm{m\,s^{-1}}$ are common over sea ice, and are often associated with a low-level jet. During periods of cold, off-ice advection, low-cloud fraction and the surface LW cloud radiative effect are enhanced over open water. This enhanced cloud radiative effect acts to substantially slow the rate of LW cooling of the ocean mixed layer compared to what would happen if low-cloud fraction were uncorrelated with warm or cold advection. Low-cloud fraction over sea ice is similar for on-ice and off-ice advection conditions, indicating that low clouds that form over the open ocean are coupled to the surface and do not survive when separated from the moisture source provided by open water.

These results support the hypothesis of two-way interactions between the ocean surface and the atmospheric boundary layer during winter over polar oceans. Regions of open water have relatively warm surface temperatures and large surface fluxes of heat and moisture to the atmosphere. Moist and warm boundary layers with a strong greenhouse effect form over open water and thus reinforce the warm surface temperatures there. If such a region were to become covered by sea ice then the surface heat and moisture fluxes would reduce

and the boundary layer would cool, dry, and become less cloudy, causing the greenhouse effect of the boundary layer to weaken. This would reinforce the cool surface temperatures and help the sea ice persist.

Additionally, 10 state-of-the-art climate models with *CALIPSO* simulator output were examined. Seven out of 10 models simulate a larger low-cloud fraction over open water than over sea ice. Nine out of 10 models underestimate low-cloud fraction over open water, and 7 out of 8 fully coupled models underestimate low-cloud fraction over sea ice. The observed low-cloud and boundary layer properties shown in this work can be used as a test in future model intercomparison projects when *CALIPSO* simulator output for more models is available.

Acknowledgments. This research was conducted with support from NASA Grant NNX14AJ26G, *Terra* and *Aqua* Science. Tsubasa Kohyama was supported by the National Science Foundation (NSF) under Grants AGS-1549579 and AGS-0960497, and the Takenaka Scholarship Foundation. We are grateful to Steve Warren for helpful discussion, Peter Blossey for sharing code for the radiative transfer model, Gregory Elsaesser for providing the MAC-LWP data, and three anonymous reviewers for their thorough and constructive feedback. We also thank the *CALIPSO* team and the authors of (Chepfer et al. 2010) for creating the *CALIPSO*-GOCCP dataset. We acknowledge the World Climate Research Programme's Working Group on Coupled Modelling, which is responsible for CMIP, and we thank the climate modeling groups for producing and making available their model output. For CMIP the U.S. Department of Energy's Program for Climate Model Diagnosis and Intercomparison provides coordinating support and led development of software infrastructure in partnership with the Global Organization for Earth System Science Portals.

APPENDIX

Derivation of 95% Confidence Interval for the Mean Low-Cloud Fraction

Figures 3b and 3e show the mean low-cloud fraction as a function of meridional distance from the sea ice edge in the Weddell Sea and Ross Sea, respectively. The 95% confidence interval for mean low-cloud fraction is computed assuming that low-cloud fraction measurements at each grid-cell and time are independent. The low-cloud fraction data are available as monthly averages on a 2° longitude by 2° latitude grid. To justify the assumption that measurements of low-cloud fraction at each grid cell and time are independent, we must assess spatial and temporal autocorrelation.

a. Serial correlation in the meridional dimension

Our goal is to bin the data by meridional distance from the ice edge and compute the mean and 95% confidence interval for the mean of each bin. The *CALIPSO* grid is resolved in 2° latitude grid cells, and when compositing by meridional distance from the ice edge we use bins of width 0.5° latitude. Therefore, for any given time, no two grid cells of the same longitude and neighboring latitudes can be assigned to the same bin. We therefore do not need to consider serial correlation in the meridional dimension when estimating the effective degrees of freedom of each bin.

b. Serial correlation in the zonal dimension

We estimate a lower bound for the number of degrees of freedom in the zonal dimension by computing the correlation length scale L for each latitude and time, and comparing it to the resolution of the *CALIPSO* grid. Following (Taylor 1921; Keller 1935), we define the correlation length scale as

$$L = \int_0^\infty r(\tau)\, d\tau$$

where $r(\tau)$ is the spatial autocorrelation function of low-cloud fraction in the zonal dimension and τ is the separation distance. The distance $2L$ can be thought of as the distance between independent points in the zonal dimension. We computed $2L$ for each time and latitude within 10 degrees of the sea ice edge, and the maximum value was an order of magnitude smaller than the 2° longitude resolution of the *CALIPSO* grid. We therefore treat each grid cell as an independent measurement of low-cloud fraction in the zonal dimension.

c. Serial correlation in the time dimension

Each longitude and latitude grid-cell contains a time series of low-cloud fraction observations. The number of effective degrees of freedom of the low-cloud fraction time series (N_{eff}) is related to the number observations of low-cloud fraction (N) and the lag-1 autocorrelation of low-cloud fraction (r_1) by the following equation (Bretherton et al. 1999):

$$\frac{N_{\text{eff}}}{N} = \frac{1 - r_1}{1 + r_1}$$

Our goal is to bin the observations of low-cloud fraction by their meridional distance from the ice edge and then to use this equation to estimate the effective degrees of

freedom for each bin. For each longitude and latitude grid cell we compute r_1 over the entire time series. Then, for a given bin, say "bin A," and a given grid cell, say "grid cell B," we keep track of the number of times that grid cell B is assigned to bin A and then compute an estimate for the number of effective degrees of freedom contributed to bin A by grid cell B by scaling by the right-hand side of the above equation. This procedure is done for every grid cell and every bin.

The total number of effective degrees of freedom for each bin estimated by this procedure is slightly greater than if one were to assume each observation of low-cloud fraction is independent in the time dimension. This happens because the lag-1 autocorrelation of low-cloud fraction over the domain tends to be slightly negative, probably because of random sampling variability. We therefore assume that each estimate of low-cloud fraction is independent in the time dimension.

REFERENCES

Ackerman, S., R. Holz, R. Frey, E. Eloranta, B. Maddux, and M. McGill, 2008: Cloud detection with MODIS. Part II: Validation. *J. Atmos. Oceanic Technol.*, **25**, 1073–1086, doi:10.1175/2007JTECHA1053.1.

Andreas, E. L, K. J. Claffey, and P. Makshtas, 2000: Low-level atmospheric jets and inversions over the western Weddell Sea. *Bound.-Layer Meteor.*, **97**, 459–486, doi:10.1023/A:1002793831076.

Barton, N. P., S. A. Klein, J. S. Boyle, and Y. Y. Zhang, 2012: Arctic synoptic regimes: Comparing domain-wide Arctic cloud observations with CAM4 and CAM5 during similar dynamics. *J. Geophys. Res.*, **117**, D15205, doi:10.1029/2012JD017589.

Baum, B., W. Menzel, R. Frey, D. Tobin, R. Holz, S. Ackerman, A. Heidinger, and P. Yang, 2012: MODIS cloud-top property refinements for collection 6. *J. Appl. Meteor. Climatol.*, **51**, 1145–1163, doi:10.1175/JAMC-D-11-0203.1.

Blackadar, A. K., 1957: Boundary layer wind maxima and their significance for the growth of nocturnal inversions. *Bull. Amer. Meteor. Soc.*, **38**, 283–290.

Boisvert, L. N., and J. C. Stroeve, 2015: The Arctic is becoming warmer and wetter as revealed by the Atmospheric Infrared Sounder. *Geophys. Res. Lett.*, **42**, 4439–4446, doi:10.1002/2015GL063775.

Bourassa, M. A., and Coauthors, 2013: High-latitude ocean and sea ice surface fluxes: Challenges for climate research. *Bull. Amer. Meteor. Soc.*, **94**, 403–423, doi:10.1175/BAMS-D-11-00244.1.

Bracegirdle, T. J., and G. J. Marshall, 2012: The reliability of Antarctic tropospheric pressure and temperature in the latest global reanalyses. *J. Climate*, **25**, 7138–7146, doi:10.1175/JCLI-D-11-00685.1.

Bretherton, C. S., M. Widmann, V. P. Dymnikov, J. M. Wallace, and I. Bladé, 1999: The effective number of spatial degrees of freedom of a time-varying field. *J. Climate*, **12**, 1990–2009, doi:10.1175/1520-0442(1999)012<1990:TENOSD>2.0.CO;2.

Bromwich, D. H., J. P. Nicolas, and A. J. Monaghan, 2011: An assessment of precipitation changes over Antarctica and the Southern Ocean since 1989 in contemporary global reanalyses. *J. Climate*, **24**, 4189–4209, doi:10.1175/2011JCLI4074.1.

——, and Coauthors, 2012: Tropospheric clouds in Antarctica. *Rev. Geophys.*, **50**, RG1004, doi:10.1029/2011RG000363.

CALIPSO, 2015: CFMIP-Obs: Cloud observations for model evaluation (GOCCP, subset: monthly, June 2006–August 2014). Accessed 1 January 2016. [Available online at http://climserv.ipsl.polytechnique.fr/cfmip-obs/.]

Cesana, G., and Coauthors, 2016: Using in situ airborne measurements to evaluate three cloud phase products derived from CALIPSO. *J. Geophys. Res. Atmos.*, **121**, 5788–5808, doi:10.1002/2015JD024334.

Chepfer, H., S. Bony, D. Winker, M. Chiriaco, J.-L. Dufresne, and G. Sèze, 2008: Use of CALIPSO lidar observations to evaluate the cloudiness simulated by a climate model. *Geophys. Res. Lett.*, **35**, L15704, doi:10.1029/2008GL034207.

——, ——, ——, G. Cesana, J. L. Dufresne, P. Minnis, C. J. Stubenrauch, and S. Zeng, 2010: The GCM-oriented CALIPSO cloud product (CALIPSO-GOCCP). *J. Geophys. Res.*, **115**, D00H16, doi:10.1029/2009JD012251.

Clough, S. A., M. W. Shephard, E. J. Mlawer, J. S. Delamere, M. J. Iacono, K. Cady-Pereira, S. Boukabara, and P. D. Brown, 2005: Atmospheric radiative transfer modeling: A summary of the AER codes. *J. Quant. Spectrosc. Radiat. Transfer*, **91**, 233–244, doi:10.1016/j.jqsrt.2004.05.058.

Dee, D. P., and Coauthors, 2011: The ERA-Interim reanalysis: Configuration and performance of the data assimilation system. *Quart. J. Roy. Meteor. Soc.*, **137**, 553–597, doi:10.1002/qj.828.

Dufresne, J. L., and S. Bony, 2008: An assessment of the primary sources of spread of global warming estimates from coupled atmosphere–ocean models. *J. Climate*, **21**, 5135–5144, doi:10.1175/2008JCLI2239.1.

Eastman, R., and S. G. Warren, 2010: Interannual variations of Arctic cloud types in relation to sea ice. *J. Climate*, **23**, 4216–4232, doi:10.1175/2010JCLI3492.1.

ECMWF, 2015: ERA-Interim (subset: monthly, June 2006–August 2014). Accessed 1 January 2016. [Available online at http://apps.ecmwf.int/datasets/.]

Fitzpatrick, M. F., and S. G. Warren, 2007: The relative importance of clouds and sea ice for the solar energy budget of the Southern Ocean. *J. Climate*, **20**, 941–954, doi:10.1175/JCLI4040.1.

Gates, W. L., 1992: AMIP: The Atmospheric Model Intercomparison Project. *Bull. Amer. Meteor. Soc.*, **73**, 1962–1970, doi:10.1175/1520-0477(1992)073<1962:ATAMIP>2.0.CO;2.

Gordon, A. L., 1991: Two stable modes of Southern Ocean winter stratification. *Deep Convection and Deep Water Formation in the Oceans*, P. C. Chu and J. C. Gascard, Eds., Elsevier Oceanography Series, Vol. 57, Elsevier, 17–35.

Hartmann, D. L., 2016: *Global Physical Climatology*. 2nd ed. Academic Press, 498 pp.

Hu, Y., S. Rodier, K. Xu, W. Sun, J. Huang, B. Lin, P. Zhai, and D. Josset, 2010: Occurrence, liquid water content, and fraction of supercooled water clouds from combined CALIOP/IIR/MODIS measurements. *J. Geophys. Res.*, **115**, D00H34, doi:10.1029/2009JD012384.

Iacono, M. J., J. S. Delamere, E. J. Mlawer, M. W. Shephard, S. A. Clough, and W. D. Collins, 2008: Radiative forcing by long-lived greenhouse gases: Calculations with the AER radiative transfer models. *J. Geophys. Res.*, **113**, D13103, doi:10.1029/2008JD009944.

Johnson, G. C., 2008: Quantifying Antarctic Bottom Water and North Atlantic Deep Water volumes. *J. Geophys. Res.*, **113**, C05027, doi:10.1029/2007JC004477.

Jones, R. W., I. A. Renfrew, A. Orr, B. G. M. Webber, D. M. Holland, and M. A. Lazzara, 2016: Evaluation of four global reanalysis products using in situ observations in the Amund-

sen Sea Embayment, Antarctica. *J. Geophys. Res. Atmos.*, **121**, 6240–6257, doi:10.1002/2015JD024680.

Kapsch, M.-L., R. G. Graversen, and M. Tjernström, 2013: Springtime atmospheric energy transport and the control of Arctic summer sea-ice extent. *Nat. Climate Change*, **3**, 744–748, doi:10.1038/nclimate1884.

Karlsson, J., and G. Svensson, 2011: The simulation of Arctic clouds and their influence on the winter surface temperature in present-day climate in the CMIP3 multi-model dataset. *Climate Dyn.*, **36**, 623–635, doi:10.1007/s00382-010-0758-6.

Kay, J. E., and A. Gettelman, 2009: Cloud influence on and response to seasonal Arctic sea ice loss. *J. Geophys. Res.*, **114**, D18204, doi:10.1029/2009JD011773.

Keller, L. B., 1935: Expanding of limit theorems of probability theory on functions with continuous arguments (in Russian). *Works Main Geophys. Observ.*, **4**, 5–19.

König-Langlo, G., 2005: Meteorological observations during POLARSTERN cruise ANT-X/4. Alfred Wegener Institute, Helmholtz Center for Polar and Marine Research, Bremerhaven, doi:10.1594/PANGAEA.269526.

——, 2013: Meteorological observations during POLARSTERN cruise ANT-XXIX/6 (AWECS). Alfred Wegener Institute, Helmholtz Center for Polar and Marine Research, Bremerhaven, doi:10.1594/PANGAEA.819610.

——, B. Loose, and B. Bräuer, 2006: 25 Years of POLARSTERN Meteorology. WDC-MARE Rep., 137 pp., doi:10.2312/wdc-mare.2006.4.

Liu, Q., G. W. K. Moore, K. Tsuboki, and I. A. Renfrew, 2006: The effect of the sea-ice zone on the development of boundary-layer roll clouds during cold air outbreaks. *Bound.-Layer Meteor.*, **118**, 557–581, doi:10.1007/s10546-005-6434-4.

Liu, Y., J. R. Key, R. A. Frey, S. A. Ackerman, and W. P. Menzel, 2004: Nighttime polar cloud detection with MODIS. *Remote Sens. Environ.*, **92**, 181–194, doi:10.1016/j.rse.2004.06.004.

Marshall, J., and K. Speer, 2012: Closure of the meridional overturning circulation through Southern Ocean upwelling. *Nat. Geosci.*, **5**, 171–180, doi:10.1038/ngeo1391.

McCoy, D. T., D. L. Hartmann, and D. P. Grosvenor, 2014: Observed Southern Ocean cloud properties and shortwave reflection. Part I: Calculation of SW flux from observed cloud properties. *J. Climate*, **27**, 8836–8857, doi:10.1175/JCLI-D-14-00287.1.

Mlawer, E. J., S. J. Taubman, P. D. Brown, M. J. Iacono, and S. A. Clough, 1997: RRTM, a validated correlated-k model for the longwave. *J. Geophys. Res.*, **102**, 16 663–16 682, doi:10.1029/97JD00237.

Morrison, A. E., S. T. Siems, and M. J. Manton, 2011: A three-year climatology of cloud-top phase over the Southern Ocean and North Pacific. *J. Climate*, **24**, 2405–2418, doi:10.1175/2010JCLI3842.1.

NOAA/NSIDC, 2015: NOAA/NSIDC Climate Data Record of Passive Microwave Sea Ice Concentration, version 2 subset: Monthly, June 2006–August, 2014. National Snow and Ice Data Center, accessed 1 January 2016. [Available online at http://nsidc.org/data/G02202.]

Palm, S. P., S. T. Strey, J. Spinhirne, and T. Markus, 2010: Influence of Arctic sea ice extent on polar cloud fraction and vertical structure and implications for regional climate. *J. Geophys. Res.*, **115**, D21209, doi:10.1029/2010JD013900.

Papritz, L., S. Pfahl, H. Sodemann, and H. Wernli, 2015: A climatology of cold air outbreaks and their impact on air–sea heat fluxes in the high-latitude South Pacific. *J. Climate*, **28**, 342–364, doi:10.1175/JCLI-D-14-00482.1.

Peng, G., W. N. Meier, D. J. Scott, and M. H. Savoie, 2013: A long-term and reproducible passive microwave sea ice concentration data record for climate studies and monitoring. *Earth Syst. Sci. Data*, **5**, 311–318, doi:10.5194/essd-5-311-2013.

Petersen, G. N., and I. A. Renfrew, 2009: Aircraft-based observations of air–sea fluxes over Denmark Strait and the Irminger Sea during high wind speed conditions. *Quart. J. Roy. Meteor. Soc.*, **135**, 2030–2045, doi:10.1002/qj.355.

Renfrew, I. A., and G. W. K. Moore, 1999: An extreme cold-air outbreak over the Labrador Sea: Roll vortices and air–sea interaction. *Mon. Wea. Rev.*, **127**, 2379–2394, doi:10.1175/1520-0493(1999)127<2379:AECAOO>2.0.CO;2.

Schweiger, A. J., R. W. Lindsay, S. Vavrus, and J. A. Francis, 2008: Relationships between Arctic sea ice and clouds during autumn. *J. Climate*, **21**, 4799–4810, doi:10.1175/2008JCLI2156.1.

Screen, J. A., and I. Simmonds, 2010: The central role of diminishing sea ice in recent Arctic temperature amplification. *Nature*, **464**, 1334–1337, doi:10.1038/nature09051.

Serreze, M. C., A. P. Barrett, J. C. Stroeve, D. N. Kindig, and M. M. Holland, 2009: The emergence of surface-based Arctic amplification. *Cryosphere*, **3**, 11–19, doi:10.5194/tc-3-11-2009.

Talley, L. D., 2013: Closure of the global overturning circulation through the Indian, Pacific, and Southern Oceans: Schematics and transports. *Oceanography*, **26**, 80–97, doi:10.5670/oceanog.2013.07.

Taylor, G. I., 1921: Diffusion by continuous movement. *Proc. London Math. Soc.*, **20**, 196–212.

Taylor, K. E., R. J. Stouffer, and G. A. Meehl, 2012: An overview of CMIP5 and the experiment design. *Bull. Amer. Meteor. Soc.*, **93**, 485–498, doi:10.1175/BAMS-D-11-00094.1.

Taylor, P. C., S. Kato, K.-M. Xu, and M. Cai, 2015: Covariance between Arctic sea ice and clouds within atmospheric state regimes at the satellite footprint level. *J. Geophys. Res. Atmos.*, **120**, 12 656–12 678, doi:10.1002/2015JD023520.

Thorpe, A. J., and T. H. Guymer, 1977: The nocturnal jet. *Quart. J. Roy. Meteor. Soc.*, **103**, 633–653, doi:10.1002/qj.49710343809.

Trenberth, K. E., and J. T. Fasullo, 2010: Simulation of present-day and twenty-first-century energy budgets of the southern oceans. *J. Climate*, **23**, 440–454, doi:10.1175/2009JCLI3152.1.

Wadhams, P., M. A. Lange, and S. F. Ackley, 1987: The ice thickness distribution across the Atlantic sector of the Antarctic Ocean in midwinter. *J. Geophys. Res.*, **92**, 14535–14552, doi:10.1029/JC092iC13p14535.

Walter, B. A., 1980: Wintertime observations of roll clouds over the Bering Sea. *Mon. Wea. Rev.*, **108**, 2024–2031, doi:10.1175/1520-0493(1980)108<2024:WOORCO>2.0.CO;2.

Winker, D. M., W. H. Hunt, and M. J. McGill, 2007: Initial performance assessment of CALIOP. *Geophys. Res. Lett.*, **34**, L19803, doi:10.1029/2007GL030135.

Zhang, M. H., and Coauthors, 2005: Comparing clouds and their seasonal variations in 10 atmospheric general circulation models with satellite measurements. *J. Geophys. Res.*, **110**, D15S02, doi:10.1029/2004JD005021.